

# Towards Spatial Equilibrium Object Detection

Zhaohui Zheng    Yuming Chen    Qibin Hou\*    Xiang Li    Ming-Ming Cheng  
 TMCC, CS, Nankai University

## Abstract

Semantic objects are unevenly distributed over images. In this paper, we study the spatial disequilibrium problem of modern object detectors and propose to quantify this “spatial bias” by measuring the detection performance over zones. Our analysis surprisingly shows that the spatial imbalance of objects has a great impact on the detection performance, limiting the robustness of detection applications. This motivates us to design a more generalized measurement, termed *Spatial equilibrium Precision (SP)*, to better characterize the detection performance of object detectors. Furthermore, we also present a *spatial equilibrium label assignment (SELA)* to alleviate the spatial disequilibrium problem by injecting the prior spatial weight into the optimization process of detectors. Extensive experiments on PASCAL VOC, MS COCO, and 3 application datasets on face mask/fruit/helmet images demonstrate the advantages of our method. Our findings challenge the conventional sense of object detectors and show the indispensability of spatial equilibrium. We hope these discoveries would stimulate the community to rethink how an excellent object detector should be. All the source code, evaluation protocols, and the tutorials are publicly available at <https://github.com/Zzh-tju/ZoneEval>.

## 1. Introduction

Object detection, as one of the most popular vision tasks, has been explored deeply over the past two decades [4, 30, 37, 38]. Many endeavors have been made to push the benchmark ranking to a new level [1, 2, 18, 23, 25, 51, 60]. This paper does not aim to present a new object detector but reveals the spatial disequilibrium problem in object detection, which is mainly caused by the spatial imbalance of object distribution, as shown at the top of Fig. 1. This refers to the photographer’s bias, which has been widely demonstrated to be intrinsic in the human’s biological visual system [42, 45]. The photographers are more likely to place the important and interesting objects at the center of the viewfinder. It is natural, saliency-driven, related to

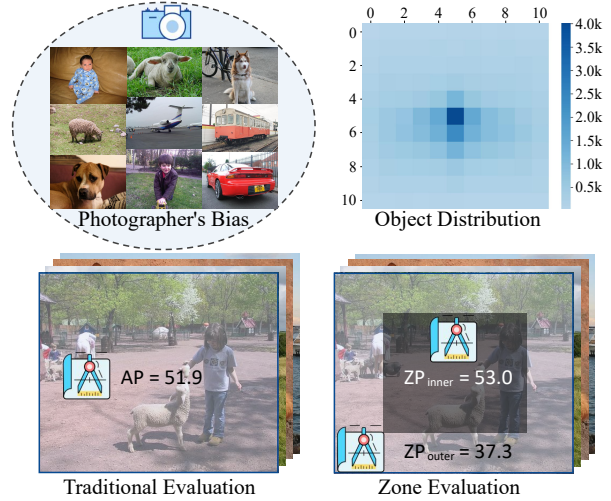


Figure 1. Top row: Photographer’s bias causes spatial imbalance of object distribution. We count the center points of all the ground-truth boxes. The images are divided into  $11 \times 11$  zones. Bottom row: The detection performance is measured by the traditional evaluation (Average Precision) and our zone evaluation (ZP, the average precision constrained in the zone). We show there is a large performance gap between zones. The results are reported by GFocal [25] on the VOC 2007 test set.

the viewing strategy, and found to be present in most of the existing visual datasets [10, 21, 29, 34, 39, 44]. The majority of objects are intensively distributed over the middle zones. This motivates us to investigate whether such photographer’s bias affects the detection performance and, if so, how much.

The core of this paper is a new zone evaluation protocol, which attempts to measure the detector’s performance over zones. The new zone precision (ZP) calculates the common Average Precision within a designated zone, where only the boxes whose centers lie in the zone are considered. With the concept of ZP, it is possible to analyze the spatial disequilibrium problem of various detectors over different image zones. As shown in Fig. 1, the ZP gap is 15.7 between the inner zone and the outer one. This performance gap indicates that the detector cannot perform uniformly across the zones, which we refer to “spatial bias”. It can be concluded

\*Corresponding author

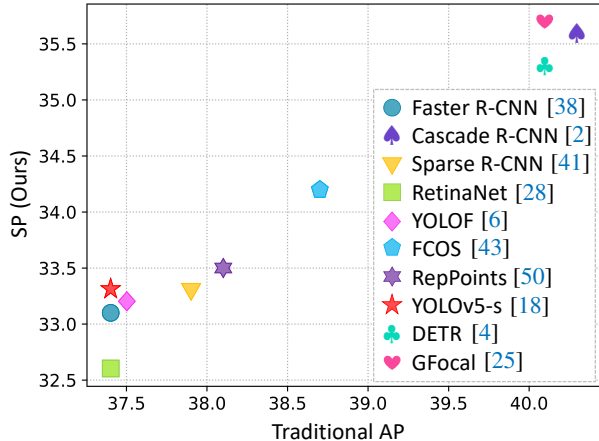


Figure 2. Spatial equilibrium Precision (SP) vs. traditional Average Precision (AP) for various object detection methods on COCO. Our SP considers the spatial equilibrium of detectors.

from the experimental results that the spatial bias is correlated to the spatial object distribution. As a result, when the object distribution satisfies the centralized photographer’s bias, the detector will behave much better in the central zone than in the outside zones. This makes the traditional metrics, such as the popular Average Precision (AP), actually be inflated, heavily rely on the detection performance in a small central zone, and hence fail to evaluate the spatial robustness of object detectors.

Driven by these findings, we present a new overall metric based on ZP, called Spatial equilibrium Precision (SP), to evaluate the object detectors in a spatial equilibrium manner. More than the traditional AP, SP can reflect the spatial robustness of detectors and reduce the over-reliance on the small central zone. With SP, we show surprising results where the benchmark ranking changes. As shown in Fig. 2, YOLOv5-s [18] produces the lowest traditional AP among these detectors. However, a higher SP score is achieved by YOLOv5-s since it performs much better in terms of spatial equilibrium, even on par with Sparse R-CNN [41] which gets a traditional AP of 37.9%. These results challenge our conventional understanding of the object detectors and the spatial equilibrium should not be overlooked.

Moreover, as a preliminary attempt, we propose a Spatial Equilibrium Label Assignment (SELA) to re-balance the sampling process over the zones. It successfully shrinks the performance gap between the central zone and the ones near the image borders, achieving a much better spatial equilibrium. Experimental results on PASCAL VOC [10] and MS COCO [29] support our analysis and conclusions. We also conduct experiments on 3 application datasets, including face mask/fruit/helmet images. We hope our work has implications for promoting the comprehensiveness and robustness of object detection.

## 2. Related Work

### 2.1. Data Imbalance Problem

Data imbalance is a common problem in object detection. Let  $\{X, G\} = \{x_i, g_i\}_{i=1}^n$  be a collection of sample-label pairs, where each sample  $x_i$  has a set of ground-truth labels  $g_i$ . The model training is conducted on the subset of  $\{X, G\}$ , and the network glances through the training set at each training epoch. The data imbalance problems are usually related to the inherent properties of  $\{X, G\}$ . In the literature of object detection, there are mainly two widely discussed imbalance problems.

**Class imbalance problem.** In this case, the sample  $X$  is composed of multiple subsets  $X_1, X_2, \dots, X_c$  according to the class division, where the number of samples is imbalanced across  $c$  classes, thereby yielding a long-tail distribution [26, 35, 47, 54]. The class imbalance problem naturally causes imbalanced sampling during training, hindering the classification performance for those tail classes. Re-sampling strategies [19, 33] and cost-sensitive learning [8, 55] are the mainstream paradigms for class re-balancing.

**Foreground-background sampling imbalance.** This imbalance is also derived from the data itself. A large number of anchor points are tiled on the background area, which are naturally sampled to be the negatives and hence dominant the gradient flows. In this case,  $X$  can be split into  $X_n$  and  $X_p$ , s.t.,  $X = X_n \cup X_p$ . The negative samples  $X_n$  can be seen as the complementary set of the positives  $X_p$ , whose ground-truth labels are “background” without bounding box annotations. The solutions to this problem are similar, including re-sampling, *e.g.*, OHEM [40], Guided Anchoring [46] and IoU-balanced sampling [36], and cost-sensitive learning, *e.g.*, Focal loss [28], GHM loss [22], and PISA [3].

In this work, we consider the photographer’s bias [42, 45] where objects tend to be photographed in the central zone of an image. In this case, the sample  $X$  can be divided into multiple subsets according to the spatial zones, just like the class division. Generally speaking, spatial imbalance shares the similar characteristics to class imbalance. The difference is that the latter has a long-tail distribution across classes, while the former considers the uneven distribution of objects over spatial zones.

### 2.2. Label Assignment

As a key component of object detectors, label assignment determines the positive and negative samples for detectors to learn. Early works [28, 30, 37, 38] mostly adopt a fixed label assignment strategy, *e.g.*, the max-IoU assigner, which is popular for years. Later, FCOS [43] introduces the center sampling mechanism to select the samples near the center point of the objects as the positives, and a scale as-

signment is used to assign the appropriate FPN-level for the objects with different scales.

Recently, dynamic label assignment has attracted more and more research attentions. In FSAF [58], a dynamic FPN-level selection module is proposed. FreeAnchor [53], SAPD [57], Auto-Assign [56], MuSu [12], and DW [24] all adopt the prediction-guided loss weighting method, which can be regarded as a soft label assignment strategy. By modeling the positive and negative anchors as a Gaussian Mixture Model, PAA [20] utilizes the EM algorithm [9] to conduct label assignment. OTA/SimOTA [13, 14] considers label assignment as an Optimal Transport Problem. ATSS [52] reveals an important fact that the performance gap between dense anchor-based and anchor-free detectors lies in label assignment. It takes advantage of the statistical characteristics of all the objects, and calculates the data-related IoU to assign the labels. Based on ATSS, TOOD [11] and DDOD [7] study the task-aligned and task-disentangle label assignment, respectively.

Among all the aforementioned methods, they mainly consider the instance-level information, *e.g.*, the prediction quality, the prior knowledge of objects, while neglecting the object distribution in the scene. In our work, we take this into account and propose a spatial equilibrium label assignment to tackle the spatial disequilibrium problem. Our intention is to train spatial equilibrium object detectors.

### 3. Zone Evaluation for Object Detection

As mentioned in Sec. 1, detector trained on dataset with imbalanced object distribution has different performance in different image zones. In this section, we extend the traditional object detection evaluation methods by introducing a more comprehensive zone evaluation process.

Given a test image  $I$  and a set of evaluation metrics  $\mathcal{M}$ , the classic evaluation methods simultaneously calculate the metrics for all the detections and the ground-truths over the whole image. The elements in  $\mathcal{M}$  can be the COCO-style AP (Average Precision) [29], mAP across 10 IoU thresholds, or AP for the small/medium/large objects, which have been widely used in object detection. These traditional evaluation metrics measure the detection performance over the whole image zone but consider nothing about the spatial robustness of object detectors.

**Zone metric.** Let  $z^1, z^2, \dots, z^n \in I$  be a set of disjoint image zones with union  $I$ . We measure the detection performance for a specific zone  $z^i$  by only considering the ground-truth objects and the detections whose centers lie in the zone  $z^i$ . Then, for an arbitrary evaluation metric  $m \in \mathcal{M}$ , the evaluation process stays the same to the conventional ways, yielding  $n$  zone metrics, each of which is denoted by  $m^i$ .

In practice, considering the widespread photographer’s

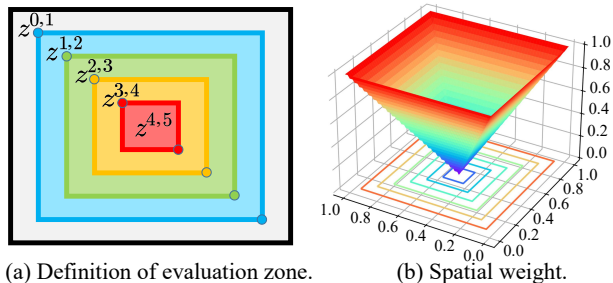


Figure 3. The definition of evaluation zones and the spatial weight in the normalized image space.

bias in the object detection datasets, as shown in Fig. 1, the evaluation zones are designed to be a series of annular areas:

$$z^{i,j} = R_i \setminus R_j, \quad i < j \quad (1)$$

where  $R_i$  denotes a centralized region, which is given by:

$$R_i = \text{Rectangle}((r_i W, r_i H), ((1 - r_i) W, (1 - r_i) H)), \quad (2)$$

where  $\text{Rectangle}(p, q)$  represents the rectangle region with the top-left coordinate  $p$  and the bottom-right coordinate  $q$ .  $W$  and  $H$  denote the width and the height of the image and  $r_i = \frac{i}{2n}, i \in \{0, 1, \dots, n\}$  controls the sizes of rectangles. An illustration of the evaluation zones can be seen in Fig. 3(a), where  $n = 5$ . We denote the range of the annular zone  $z^{i,j}$  as  $(r_i, r_j)$  for brevity. And we denote the average precision (AP) in the zone  $z^{i,j}$  as  $ZP^{i,j}$ .

**Rethinking traditional AP.** Understanding the deficiency of the traditional AP is crucial for better applying object detectors to downstream applications. It can be seen that the traditional AP is a special case in the proposed zone metric when  $i = 0$  and  $j = n$ , which corresponds to  $ZP^{0,n}$ . This metric is difficult to capture the spatial bias, and is also dominated by the detection performance in a tiny zone. To investigate its deficiency, we conduct evaluation on GFocal [25] with VOC 07+12 protocol. We design a series of evaluation zones with range  $(r_i, r_j)$ , where the number of zones  $n = 10$ ,  $r_i$  is fixed as 0 and  $r_j = 0.05j, j \in \{1, 2, \dots, 10\}$ . In a nutshell, all the evaluation zones can be regarded as hollowing the central zones  $R_j$  in the full-map zone. Fig. 4 shows us quite surprising results that when  $r_j < 0.5$ , all the ZPs are less than the traditional AP ( $r_j = 0.5$ ). Notice that even if a small central zone is excluded ( $r_j = 0.45$ ), which occupies only 1% of the whole image area, the detection performance in the remaining 99% zones can only produce 46.7 ZP, much lower than the traditional one. This exposes the defects of traditional metrics. They are actually inflated and largely dominated by the detection performance in a small central zone. Due to this fact, the traditional metrics can hardly reflect the real overall performance of the detectors.

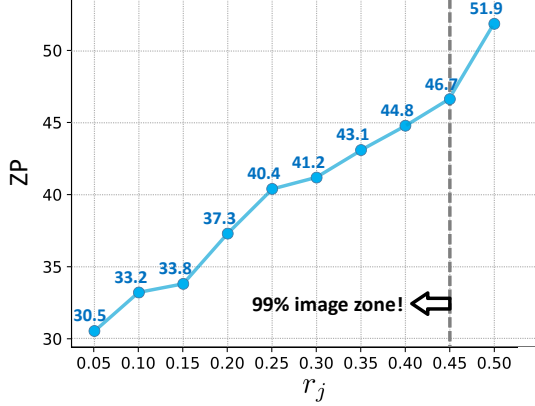


Figure 4. ZP scores against the zone range  $(r_i, r_j)$ , where  $r_i$  is fixed as 0, and  $r_j = 0.05j$ ,  $j \in \{1, 2, \dots, 10\}$ . We can see that even if a small central zone is excluded ( $r_j = 0.45$ ), which occupies only 1% of the whole image area, the detection performance in the remaining 99% zones can only produce 46.7 ZP, much lower than the traditional AP score over the whole image zone.

**Spatial equilibrium metrics.** Motivated by the aforementioned analysis, here, we attempt to propose a spatial equilibrium metric, which considers both the zone metrics and the zone areas to better reflect the detection performance. Considering the normalized image space (square image with unit area 1), the spatial equilibrium metric for a given metric  $m$  is given by:

$$Sm = \sum_i \text{Area}(z^i) \cdot m^i, \quad (3)$$

where  $\text{Area}(\cdot)$  calculates the area of the zone. In this way, the spatial equilibrium metric  $Sm$  is a weighted sum of the zone metrics. One may note that the spatial equilibrium metric is based on an assumption similar to the traditional metric, i.e., the detector performs uniformly in the zone. The difference is, our spatial equilibrium metric applies this assumption to a series of smaller zones, rather than the full map for traditional metrics.

Table 1. Notations of different evaluation metrics.

Notation	Descriptions
$ZP^{i,j}$	Average Precision (AP) in $z^{i,j}$ .
$mZP^{i,j}$	mAP under a given IoU threshold in $z^{i,j}$ .
$ZP_{75}^{i,j}$	AP <sub>75</sub> in $z^{i,j}$ .
SP	Spatial equilibrium metric for ZP.
SP <sub>75</sub>	Spatial equilibrium metric for ZP <sub>75</sub> .

**Notations.** For simplicity, the notations can be seen in Table 1. In the experiments, SP should be considered as the most important metric for characterizing the detection performance.

**Measuring the discrete amplitude for zone metrics.** As the detection performance varies across the zones, we fur-

ther introduce an additional metric to gauge the discrete amplitude among the zone metrics. Given all the zone metrics for  $m$ , we calculate the variance of the zone metrics,

$$\sigma(m) = \frac{\sum_i (m^i - \bar{m})^2}{n}, \quad (4)$$

where  $\bar{m} = \sum_i m^i / n$  denotes the mean value of the zone metrics, and  $n$  denotes the number of zones. Ideally, if  $\sigma(m) = 0$ , the object detector reaches perfectly spatial equilibrium under the current zone division. In this situation, an object can be well detected without being influenced by its spatial position.

## 4. Spatial Equilibrium Label Assignment

Re-sampling is one of the promising solutions to enhance the robustness of object detectors. It is also widely used for alleviating the long-tail class imbalance. For example, increasing sampling frequency for the tail classes can provide more training samples for the network to generalize better. We, in this work, propose a simple yet effective Spatial Equilibrium Label Assignment (SELA) to relieve the issue of spatial disequilibrium. We first introduce the key component of our method—the spatial weight. We map the anchor point coordinate  $(x^a, y^a)$  to a spatial weight  $\alpha(x^a, y^a)$  by a spatial weighting function,

$$\alpha(x, y) = 2 \max \left\{ \left\| x - \frac{W}{2} \right\|_1 \frac{1}{W}, \left\| y - \frac{H}{2} \right\|_1 \frac{1}{H} \right\}, \quad (5)$$

where  $W$  and  $H$  are the width and the height of the image. The spatial weight has the following properties:

- Non-negativity;
- Bounded by  $[0, 1]$ ;
- $\lim_{(x,y) \rightarrow (\frac{W}{2}, \frac{H}{2})} \alpha(x, y) = 0$ ;
- When  $p$  is located at the image border, we have  $\lim_{(x,y) \rightarrow p} \alpha(x, y) = 1$ .

An illustration of the spatial weight can be seen in Fig. 3(b). Next, we show how to use the spatial weight defined in Eq. 5 to improve the classic detectors.

**Usage of spatial weight.** The spatial weight can be easily plugged into the existing label assignment algorithms. The principle is simple and multi-optional. The key idea is to consider the spatial weight as an additional constraint term when making the criterion rule for label assignment. Since most of the label assignment algorithms have their own sophisticated implementations, in the following, we provide a specific application description of the classic ATSS [52],

simply because of its brevity. Given the positive IoU threshold  $t$ , which is calculated by considering the statistical characteristics of the objects. The ATSS criterion follows the same rule as the max-IoU assignment [28, 37, 38],

$$\text{IoU}(B^a, B^{gt}) \geq t, \quad (6)$$

where  $B^a$  and  $B^{gt}$  denote the preset anchor boxes and the ground-truth boxes. Our SELA process is represented as:

$$\text{IoU}(B^a, B^{gt}) \geq t - \gamma\alpha(x^a, y^a), \quad (7)$$

where  $\gamma \geq 0$  is a hyperparameter. It can be seen that SELA relaxes the positive sample selection conditions for objects near the image borders. Therefore, more anchor points will be selected as the positive samples for them.

**Discussions.** Notice that the above simple application is actually a frequency-based approach, just like many of the class re-balance sampling strategies proposed for the long-tail class imbalance problem [19, 33]. This is not the unique option to pursue spatial equilibrium. Cost-sensitive learning [8, 55] is also worth considering. We exploit the spatial weight to enlarge the loss weight for positive samples. Thus, a larger gradient flow will be generated for the outer zones to make the network focus more on the objects away from the center. Besides, there are some potentially promising solutions toward spatial equilibrium that deserve further study. For example, designing an appropriate data augmentation, more specifically, increasing data augmentation to make up the insufficient sampling frequency for the objects near the image borders, might be a promising solution toward spatial equilibrium. Also, we can actually design a skew spatial weight if the data has a skew object distribution. We leave them for future research.

Table 2. Brief information of the datasets for training and test.

Dataset	Training	Test	#Classes	Source
PASCAL VOC	16,551	4,952	20	[10]
MS COCO	118K	5,000	80	[29]
Face mask	5,865	1,035	2	Kaggle
Fruit	3,836	639	11	Kaggle
Helmet	15,887	6,902	2	Kaggle

## 5. Experiment

We conduct extensive experiments on various object detectors and 5 detection datasets, including PASCAL VOC [10] MS COCO [29], and 3 public application datasets (face mask/fruit/helmet images). The experiments contain two parts, the zone evaluation and the SELA evaluation.

### 5.1. Implementation Details

For zone evaluation, we follow the standard Average Precision evaluation protocols. All the object detectors we

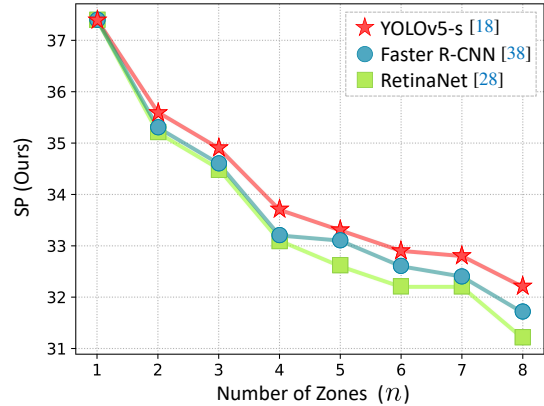


Figure 5. Spatial equilibrium Precision (SP) against the number of zones.  $n = 1$  denotes the traditional full map evaluation. We set  $n = 5$  by default. The results are reported on COCO 2017 val.

evaluate can be downloaded from MMDetection [5] or their official websites. To comprehensively evaluate the detectors and our SELA, various metrics are reported, including the SP, 5 zone metrics, the variance of 5 zone metrics, and the traditional metrics. Unless otherwise stated, we adopt  $n = 5$  for the zone division, which can be seen in Fig. 3(a). The types of the evaluation metrics follow the standard protocols, i.e., AP (Average Precision) and AP<sub>75</sub>, thereby yielding SP, SP<sub>75</sub>, ZP, ZP<sub>75</sub>, etc.

For the usage of datasets, we adopt the classical VOC 07+12 training and test protocols for PASCAL VOC. The training set contains the union of VOC 2007 trainval and VOC 2012 trainval and the test set contains VOC 2007 test. For MS COCO, we adopt COCO 2017 train (118K images) for training and COCO 2017 val (5K images) for evaluation. Moreover, we adopt the VOC-style training and test protocols for 3 application datasets. All the datasets we used are publicly available, and can be downloaded from their official websites or Kaggle. The brief information is listed in Table 2. More details can be seen in the Appendix.

For SELA evaluation, the implementation is based on the popular dense object detector GFocal [25] with ResNet [17] backbone and FPN [27] neck under the MMDetection [5] framework. We use ResNet-18 for VOC 07+12 and 3 application datasets, and adopt ResNet-50 for MS COCO. The learning rate setting follows the linear scaling rule [15] according to the number of GPUs. The training epochs are set to 12 for all the experiments. All the other hyperparameters except  $\gamma$  in Eq. 7 remain unchanged for a fair comparison.

### 5.2. Analysis on Zone Evaluation

**Number of Zones.** We first investigate how the number of zones  $n$  affects detectors' performance. Recall that the zones are defined as a series of disjoint annular regions, and their union is the whole image. A typical illustration ( $n =$

Table 3. Performance comparison among the existing popular object detectors. The spatial equilibrium precisions (SP), 5 zone precisions (ZP), the variance of ZPs, and the traditional metrics are reported. The results are reported on COCO 2017 val. **R**: ResNet [17]. **X**: ResNeXt-32x4d [49]. **PVT-s**: Pyramid vision transformer-small [48].

Detector	SP	ZP <sup>0,5</sup>	Variance	ZP <sup>0,1</sup>	ZP <sup>1,2</sup>	ZP <sup>2,3</sup>	ZP <sup>3,4</sup>	ZP <sup>4,5</sup>
DETR ( <b>R</b> -50) [4]	35.3	40.1	26.9	29.8	36.2	39.8	39.1	45.7
RetinaNet ( <b>PVT-s</b> ) [48]	35.5	40.4	19.7	30.8	36.9	39.0	37.4	44.6
Cascade R-CNN ( <b>R</b> -50) [2]	35.6	40.3	18.7	30.9	36.6	39.2	38.6	44.2
GFocal ( <b>R</b> -50) [25]	35.7	40.1	14.4	30.9	37.2	39.1	38.3	42.5
Cascade Mask R-CNN ( <b>R</b> -101) [2]	40.3	45.4	22.4	34.7	41.6	44.3	44.4	49.1
Sparse R-CNN ( <b>R</b> -50) [41]	40.6	45.0	21.6	35.8	41.9	43.4	44.0	50.3
YOLOv5-m [18]	40.8	45.2	12.9	36.0	42.3	44.5	43.2	46.7
Mask R-CNN ( <b>Swin-T</b> ) [31]	40.9	46.0	15.4	36.8	41.7	44.1	43.5	49.0
Mask R-CNN ( <b>ConvNeXt-T</b> ) [32]	41.1	46.2	17.6	36.7	41.9	44.5	43.6	49.7
Cascade Mask R-CNN ( <b>X</b> -101) [2]	41.2	46.1	21.1	36.1	42.0	44.8	45.9	49.9
VFNet ( <b>R</b> -101) [51]	41.5	46.2	15.6	36.7	43.0	45.0	44.5	48.8
Deformable DETR ( <b>R</b> -50) [60]	41.6	46.1	23.2	36.3	42.6	45.6	45.1	51.2
Sparse R-CNN ( <b>R</b> -101) [41]	41.7	46.2	21.1	36.9	42.9	44.9	44.7	51.3
GFocal ( <b>X</b> -101) [25]	41.8	46.1	15.7	37.0	43.5	45.0	44.4	49.3

5) can be seen in Fig. 3(a). As shown in Fig. 5, we plot the SP curves against the number of zones for YOLOv5-s [18], Faster R-CNN [38], and RetinaNet [28]. One can see that when  $n = 1$ , our SP is identical to the traditional AP as the term  $\text{Area}(z^{0,n}) = 1$  in Eq. 3, which means that the detectors are assumed to perform uniformly in the whole image zone. As  $n$  increases, the requirements for spatial equilibrium become stricter and stricter. When  $n > 1$ , the performance gaps of these 3 detectors change. And when  $n \geq 5$ , the performance gap is distinguishable enough and the detector ranking becomes stable. Therefore, considering the metric computations, we set  $n = 5$  by default and it should be noted that a large  $n$  is also acceptable if a more rigorous spatial equilibrium is required.

**Evaluation of various object detectors.** In Table 3, we report the performance comparison for various popular detectors with the same level traditional metrics. These detectors have different detection pipelines, e.g., one-stage dense detectors (RetinaNet [28], GFocal [25], VFNet [51], YOLOv5 [18]), multi-stage dense-to-sparse detectors (R-CNN series [2, 16, 38]), and sparse detectors (DETR series [4, 60] and Sparse R-CNN [41]). One can see that GFocal and DETR achieve the same traditional AP 40.1, i.e., ZP<sup>0,5</sup>. However, GFocal performs better in the outer zones  $z^{0,1}$  and  $z^{1,2}$ , which occupy 64% image areas. Our spatial equilibrium metrics take the spatial equilibrium into account and show a 0.4 SP superiority of GFocal over DETR. Similarly, Mask R-CNN (**Swin-T**) has a comparable traditional AP to GFocal (**X**-101). One can see that GFocal performs slightly better than Mask R-CNN in the zone  $z^{0,1}$  and  $z^{4,5}$ , while significantly better in the 3 zones  $z^{1,2}$ ,  $z^{2,3}$ , and  $z^{3,4}$ , and therefore shows a 0.9 SP gap to Mask R-CNN. One more interesting is the sparse detectors, e.g., DETR series and Sparse R-CNN tend to produce a large variance,

while the one-stage dense detectors perform better in spatial equilibrium. In general, our SP encourages the detector to perform uniformly and well in all zones.

**Spatial bias in datasets.** Table 4 reports the quantitative detection results on PASCAL VOC and 3 application datasets. One can see that the detection performance varies across the zones. The zone nearest to the image border, i.e.,  $z^{0,1}$ , has the consistent lowest detection performance than the others. In contrast, the central zone  $z^{4,5}$  has the highest performance in almost all of these cases. But one should note that there is an exception such as the helmet dataset, where the ZP in the central zone  $z^{4,5}$  is not the best, but the ZP in the zone  $z^{3,4}$  is. This is because the object distribution of the helmet dataset does not satisfy the common centralized photographer’s bias. The helmets and the human heads are more likely to be in the top region of the image (kindly refer to the Appendix). As a result, the detector also shows a skew zone performance as the object distribution is skew. The amplitude of spatial disequilibrium also varies for these datasets. For examples, the variance of ZP is 49.4 on PASCAL VOC but only 3.2 on the helmet dataset.

### 5.3. Analysis on SELA

**Hyperparameter  $\gamma$ .** In Eq. 7,  $\gamma$  controls the magnitude of the spatial weight. A larger  $\gamma$  increases more positive samples for objects near the image borders. As shown in Table 5, we observe that our SELA can achieve a consistent spatial equilibrium improvement (lower variance) for all the options of  $\gamma$ . A large  $\gamma$  will increase much more positive samples for all zones, leading to a performance drop. Thus, we set  $\gamma$  to 0.2 for PASCAL VOC. One can see that our SELA can significantly improve the detection performance for the outer zones, e.g., ZP<sup>0,1</sup> and ZP<sup>1,2</sup>. To pursue spatial equilibrium, it is reasonable that the performance in the

Table 4. Evaluation of SELA for the spatial equilibrium precisions (SP), 5 zone precisions (ZP), the variance of ZPs, and the traditional metrics on 4 datasets, including VOC 07+12 and Face mask/Fruit/Helmet detection.

Dataset	SELA	Overall		$z^{0,5}$		Variance		$z^{0,1}$		$z^{1,2}$		$z^{2,3}$		$z^{3,4}$		$z^{4,5}$	
		SP	SP <sub>75</sub>	ZP	ZP <sub>75</sub>	ZP	ZP <sub>75</sub>	ZP	ZP <sub>75</sub>	ZP	ZP <sub>75</sub>	ZP	ZP <sub>75</sub>	ZP	ZP <sub>75</sub>	ZP	ZP <sub>75</sub>
VOC 07+12	✓	37.2	40.3	51.9	56.0	49.4	66.4	31.5	33.5	37.7	41.3	40.1	43.6	43.4	46.5	52.8	58.5
		38.6	41.1	52.5	57.0	37.9	58.8	33.9	34.3	38.6	42.0	41.5	45.0	43.3	47.7	52.5	57.8
Face Mask	✓	61.5	74.5	69.0	86.9	17.9	31.5	55.3	65.4	63.7	80.7	65.9	80.8	65.9	76.0	66.8	76.2
		62.8	76.5	69.1	87.5	9.1	19.4	57.9	69.6	65.5	81.8	65.9	81.8	65.2	75.8	65.0	75.9
Fruit	✓	67.0	76.1	74.7	84.1	50.9	47.7	61.9	70.9	67.9	77.8	68.3	76.5	72.9	81.5	83.3	91.7
		67.8	78.0	75.2	85.0	37.9	28.6	64.1	76.5	67.9	77.6	68.8	77.0	72.4	81.1	82.2	90.8
Helmet	✓	52.0	54.4	55.0	55.7	3.2	9.0	50.1	52.4	51.4	52.6	54.5	56.7	54.7	59.9	52.1	58.2
		52.8	55.9	55.5	56.7	2.5	6.7	51.5	54.8	52.0	53.5	54.9	58.0	55.4	60.3	52.6	59.1

Table 5. Evaluation of hyper-parameter  $\gamma$ . SP and ZPs are reported. “Var”: the variance of the 5 ZPs.  $\gamma = 0$  denotes the baseline GFocal. The results are reported on VOC 07+12.

$\gamma$	ZP <sup>0,5</sup>	ZP <sup>0,1</sup>	ZP <sup>1,2</sup>	ZP <sup>2,3</sup>	ZP <sup>3,4</sup>	ZP <sup>4,5</sup>	Var	SP
0	51.9	31.5	37.7	40.1	<b>43.4</b>	<b>52.8</b>	49.4	37.2
0.1	52.2	32.4	38.2	40.0	42.9	52.6	44.1	37.6
0.2	52.5	<b>33.9</b>	38.6	<b>41.5</b>	43.3	52.5	<b>37.9</b>	<b>38.6</b>
0.3	<b>52.6</b>	33.1	<b>39.5</b>	41.4	<b>43.4</b>	52.2	38.4	38.6
0.4	51.6	31.8	36.9	40.3	43.0	51.6	43.6	37.1

central zone  $z^{4,5}$  decreases. This is because the objects near the image borders receive more supervision signals during training, which relieves the network from paying too much attention to the central objects. Nevertheless, we believe it is acceptable since  $z^{4,5}$  occupies only 4% image areas and we aim to chase a better spatial equilibrium. In practice, we set  $\gamma = 0.1$  for all the other datasets, but it should be noted that there might be a better  $\gamma$  for different application scenarios.

**Spatial weight.** One may wonder how would the performance go if we directly loose the selection condition for the positive samples without considering their spatial positions. Here, we conduct an experiment to investigate the effect of the spatial weight. The quantitative results are reported in Table 6. If the spatial weight is set to a constant 1, which means that we directly lower the positive IoU threshold,

$$\text{IoU}(B^a, B^{gt}) \geq t - \gamma, \quad (8)$$

more positive samples will be selected without the spatial discrimination. One can see that although the ZP<sup>0,5</sup> increases, the variance of the 5 ZPs is large. This means subtracting a constant from the positive IoU threshold cannot change the sampling frequency much, since more positive samples are generated in the central zone. In contrast, our SELA can significantly reduce this variance, achieve a much better spatial equilibrium, and produce better SP.

**SELA on various datasets.** Table 4 shows us promising results that our SELA can achieve a better spatial equilibrium

Table 6. Analysis of spatial weight. SP and ZPs are reported. “Var”: the variance of the 5 ZPs.  $\gamma = 0.2$ . The results are reported on VOC 07+12.

weight	ZP <sup>0,5</sup>	ZP <sup>0,1</sup>	ZP <sup>1,2</sup>	ZP <sup>2,3</sup>	ZP <sup>3,4</sup>	ZP <sup>4,5</sup>	Var	SP
0	51.9	31.5	37.7	40.1	<b>43.4</b>	<b>52.8</b>	49.4	37.2
1	<b>52.5</b>	31.1	38.4	41.1	43.1	52.7	49.1	37.4
$\alpha(x^a, y^a)$	<b>52.5</b>	<b>33.9</b>	<b>38.6</b>	<b>41.5</b>	43.3	52.5	<b>37.9</b>	<b>38.6</b>

for object detection. In particular, we reduce the variance by a large margin in terms of ZP and ZP<sub>75</sub>. For example, we successfully lower the variance of ZP by -11.5, -8.8, -13.0 and -0.7 on PASCAL VOC, and face mask/fruit/helmet detection. More importantly, our SELA lifts the SP scores by +1.4, +1.3, +0.8, and +0.8 for the 4 datasets.

**Performance on border zones.** As SELA enhances the supervision signal in the border zones, it can be seen from Fig. 4 that the detection performance can be significantly improved for the border zones  $z^{0,1}$ . We also conduct evaluation with a finer zone division, which is the same to the settings of Fig. 4, where  $r_i, r_j$  control the range of the annual zones. As plotted in Fig. 6(a), our SELA shows a consistent ZP improvement for all the  $r_j$ , which is remarkable especially for the border zone, i.e., a small  $r_j$ .

**Correlation with object distribution.** We further provide the correlation between the zone metrics and the object distribution. We define a finer zone division, which is the same to the division for counting the centers of the objects, i.e.,  $11 \times 11$  square zones (see the top of Fig. 1). Then we evaluate the detection performance in the 121 zones one by one. To quantitatively investigate the correlation between the zone metrics and the object distribution, we calculate the Pearson Correlation Coefficient (PCC) and the Spearman Correlation Coefficient (SCC) between the mZPs and the object distribution of the test set.

As shown in Figs. 6(b) and (c), we get the following deep reflection about the spatial bias. We first note that all the PCCs  $> 0.3$  in Fig. 6(b), which indicates that the detection performance is moderately linear correlated with the object

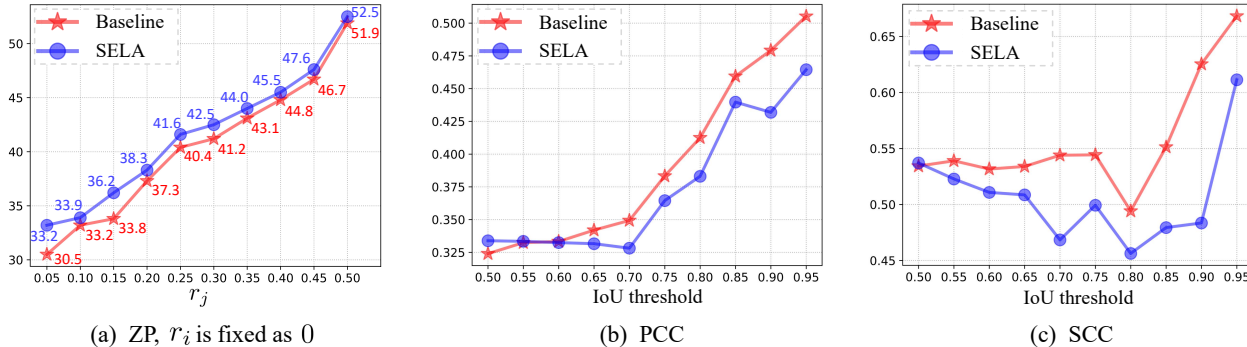


Figure 6. (a) ZP against the zone range  $(r_i, r_j)$ , where  $r_i$  is fixed as 0 and  $r_j = 0.05j$ ,  $j = \{1, 2, \dots, 10\}$ . (b) Pearson Correlation Coefficient (PCC) between the mZP and the object distribution (center counts) against the IoU threshold. (c) Spearman Correlation Coefficient (SCC) between the mZP and the object distribution against the IoU threshold. Our SELA can substantially reduce these correlations under most of IoU thresholds. The results are reported on VOC 07+12.

Table 7. Evaluation of SELA with various backbone networks on PASCAL VOC 07+12. SP and ZPs are reported. “Var”: the variance of the 5 ZPs. **R**: ResNet [17]. **X**: ResNeXt-32x4d-DCN [49, 59].

Model	SELA	ZP <sup>0,5</sup>	ZP <sup>0,1</sup>	ZP <sup>1,2</sup>	ZP <sup>2,3</sup>	ZP <sup>3,4</sup>	ZP <sup>4,5</sup>	Var	SP
<b>R-18</b>	✓	51.9	31.5	37.7	40.1	43.4	52.8	49.4	37.2
		52.5	33.9	38.6	41.5	43.3	52.5	37.9	38.6
<b>R-50</b>	✓	55.4	36.8	41.7	44.2	47.0	56.2	42.8	41.7
		55.6	39.0	42.4	45.1	46.0	54.4	22.9	42.6
<b>X-101</b>	✓	62.7	43.2	49.8	51.5	54.0	62.9	34.5	48.8
		63.0	44.6	50.3	51.9	53.5	62.9	27.4	49.5

distribution. As a reminder, the PCC only reflects the linear correlation of two given vectors, while it may fail when they are curvilinearly correlated. In Fig. 6(c), the Spearman correlation reflects a higher ranking correlation between the mZPs and the object distribution with all the SCCs > 0.45. This illustrates that the detection performance has a similar trend to the object distribution. In general, our SELA substantially reduces these correlations, indicating a lower correlation with the object distribution.

**Generality of SELA.** We first provide more experiments to verify the effectiveness of SELA on various backbone networks. Table 7 exhibits that our SELA can notably improve the spatial equilibrium for all the 3 backbone networks, i.e., lower variance and better SP. We also conduct experiments to check out the generality of SELA by incorporating it into 2 more dynamic label assignment algorithms, DW [24] and DDOD [7]. The principle of applying SELA into these detectors lies in considering the spatial weight when making the criterion rule for determining the positives and negatives. Here, we adopt a unified implementation, i.e., the cost-sensitive learning approach. We take the spatial weight term  $1 + \gamma\alpha(x^a, y^a)$  as an additional weight factor for the classification and the bounding box regression losses. Table 8 reports the quantitative results of SELA for these 3

Table 8. Evaluation of SELA (cost-sensitive learning approach) on 3 recently popular detectors with dynamic label assignments. SP and ZP<sup>0,5</sup> are reported. “Var”: the variance of ZPs over the 5 zones.

Method	SELA	VOC 07+12			COCO 2017 val		
		ZP <sup>0,5</sup>	Var	SP	ZP <sup>0,5</sup>	Var	SP
GFocal [25]	✓	51.9	49.4	37.2	40.1	14.4	35.7
		52.1	42.4	38.3	40.0	12.4	36.0
DW [24]	✓	52.6	42.8	38.2	42.0	18.8	37.2
		52.6	29.3	38.9	42.2	17.0	37.5
DDOD [7]	✓	50.8	25.1	37.4	41.7	16.3	36.8
		51.3	24.1	38.1	41.6	14.4	37.1

dynamic label assignments. As shown, our method can substantially reduce the ZP variance and improve the SP for the 3 detectors, indicating that a better spatial equilibrium is achieved. This shows the generalized ability of our method to improve the spatial robustness of detectors without bells and whistles.

## 6. Conclusions and Discussions

In this paper, we study the spatial disequilibrium problem in object detection and show the existence of the spatial bias in modern object detectors. We present a new zone evaluation protocol to quantitatively evaluate the detection performance in a series of zones. The outcome is a spatial equilibrium precision (SP), which can comprehensively evaluate the object detectors. We also present a spatial equilibrium label assignment method to alleviate the spatial disequilibrium problem of modern detectors. We hope this work could inspire the community to rethink the evaluation of object detectors and stimulate further explorations on the spatial bias.

**Discussions.** We notice that the zone division is flexible and we provide a preliminary study on the centralized zone division. The design of zone division warrants future research.



**Acknowledgement.** We would like to thank Professor Ping Wang for her valuable suggestions to this paper.

## References

- [1] Alexey Bochkovskiy, Chien-Yao Wang, and Hong-Yuan Mark Liao. Yolov4: Optimal speed and accuracy of object detection. *arXiv preprint arXiv:2004.10934*, 2020. [1](#)
- [2] Zhaowei Cai and Nuno Vasconcelos. Cascade R-CNN: Delving into high quality object detection. In *CVPR*, 2018. [1](#), [2](#), [6](#), [11](#)
- [3] Yuhang Cao, Kai Chen, Chen Change Loy, and Dahua Lin. Prime sample attention in object detection. In *CVPR*, 2020. [2](#)
- [4] Nicolas Carion, Francisco Massa, Gabriel Synnaeve, Nicolas Usunier, Alexander Kirillov, and Sergey Zagoruyko. End-to-end object detection with transformers. In *ECCV*, 2020. [1](#), [2](#), [6](#), [11](#)
- [5] Kai Chen, Jiaqi Wang, Jiangmiao Pang, Yuhang Cao, Yu Xiong, Xiaoxiao Li, Shuyang Sun, Wansen Feng, Ziwei Liu, Jiarui Xu, Zheng Zhang, Dazhi Cheng, Chenchen Zhu, Tianheng Cheng, Qijie Zhao, Buyu Li, Xin Lu, Rui Zhu, Yue Wu, Jifeng Dai, Jingdong Wang, Jianping Shi, Wanli Ouyang, Chen Change Loy, and Dahua Lin. MMDetection: Open mmlab detection toolbox and benchmark. *arXiv preprint arXiv:1906.07155*, 2019. [5](#)
- [6] Qiang Chen, Yingming Wang, Tong Yang, Xiangyu Zhang, Jian Cheng, and Jian Sun. You only look one-level feature. In *CVPR*, 2021. [2](#)
- [7] Zehui Chen, Chenhongyi Yang, Qiaofei Li, Feng Zhao, Zheng-Jun Zha, and Feng Wu. Disentangle your dense object detector. In *ACM MM*, 2021. [3](#), [8](#)
- [8] Yin Cui, Menglin Jia, Tsung-Yi Lin, Yang Song, and Serge Belongie. Class-balanced loss based on effective number of samples. In *CVPR*, 2019. [2](#), [5](#)
- [9] Arthur P Dempster, Nan M Laird, and Donald B Rubin. Maximum likelihood from incomplete data via the em algorithm. *Journal of the Royal Statistical Society: Series B (Methodological)*, 39(1):1–22, 1977. [3](#)
- [10] Mark Everingham, Luc Van Gool, Christopher K. I. Williams, John Winn, and Andrew Zisserman. The pascal visual object classes (voc) challenge. *International Journal of Computer Vision*, 88(2):303–338, 2010. [1](#), [2](#), [5](#), [11](#)
- [11] Chengjian Feng, Yujie Zhong, Yu Gao, Matthew R Scott, and Weilin Huang. TOOD: Task-aligned one-stage object detection. In *ICCV*, 2021. [3](#)
- [12] Ziteng Gao, Limin Wang, and Gangshan Wu. Mutual supervision for dense object detection. In *ICCV*, 2021. [3](#)
- [13] Zheng Ge, Songtao Liu, Zeming Li, Osamu Yoshie, and Jian Sun. OTA: Optimal transport assignment for object detection. In *CVPR*, 2021. [3](#)
- [14] Zheng Ge, Songtao Liu, Feng Wang, Zeming Li, and Jian Sun. YOLOX: Exceeding YOLO series in 2021. *arXiv preprint arXiv:2107.08430*, 2021. [3](#)
- [15] Priya Goyal, Piotr Dollár, Ross Girshick, Pieter Noordhuis, Lukasz Wesolowski, Aapo Kyrola, Andrew Tulloch, Yangqing Jia, and Kaiming He. Accurate, large mini-batch sgd: Training imagenet in 1 hour. *arXiv preprint arXiv:1706.02677*, 2017. [5](#)
- [16] Kaiming He, Georgia Gkioxari, Piotr Dollar, and Ross Girshick. Mask R-CNN. In *ICCV*, 2017. [6](#)
- [17] Kaiming He, Xiangyu Zhang, Shaoqing Ren, and Jian Sun. Deep residual learning for image recognition. In *CVPR*, 2016. [5](#), [6](#), [8](#), [11](#)
- [18] Glenn Jocher, Ayush Chaurasia, Alex Stoken, Jirka Borovec, NanoCode012, Yonghye Kwon, TaoXie, Kalen Michael, Ji-acong Fang, imyhxy, Lorna, Colin Wong, Zeng Yifu, Abhiram V, Diego Montes, Zhiqiang Wang, Cristi Fati, Je-bastin Nadar, Laughing, UnglvKitDe, tkianai, yxNONG, Piotr Skalski, Adam Hogan, Max Strobel, Mrinal Jain, Lorenzo Mammana, and xylieong. ultralytics/yolov5: v6.2 - YOLOv5 Classification Models, Apple M1, Reproducibility, ClearML and Deci.ai integrations, Aug. 2022. [1](#), [2](#), [5](#), [6](#)
- [19] Bingyi Kang, Saining Xie, Marcus Rohrbach, Zhicheng Yan, Albert Gordo, Jiashi Feng, and Yannis Kalantidis. Decoupling representation and classifier for long-tailed recognition. In *ICLR*, 2020. [2](#), [5](#)
- [20] Kang Kim and Hee Seok Lee. Probabilistic anchor assignment with iou prediction for object detection. In *ECCV*, 2020. [3](#)
- [21] Alina Kuznetsova, Hassan Rom, Neil Alldrin, Jasper Uijlings, Ivan Krasin, Jordi Pont-Tuset, Shahab Kamali, Stefan Popov, Matteo Mallocci, Alexander Kolesnikov, et al. The open images dataset v4. *International Journal of Computer Vision*, 128(7):1956–1981, 2020. [1](#)
- [22] Buyu Li, Yu Liu, and Xiaogang Wang. Gradient harmonized single-stage detector. In *AAAI*, 2019. [2](#)
- [23] Feng Li, Hao Zhang, Shilong Liu, Jian Guo, Lionel M Ni, and Lei Zhang. DN-DETR: Accelerate DETR training by introducing query denoising. In *CVPR*, 2022. [1](#)
- [24] Shuai Li, Chenheng He, Ruihuang Li, and Lei Zhang. A dual weighting label assignment scheme for object detection. In *CVPR*, 2022. [3](#), [8](#)
- [25] Xiang Li, Wenhai Wang, Lijun Wu, Shuo Chen, Xiaolin Hu, Jun Li, Jinhui Tang, and Jian Yang. Generalized Focal Loss: learning qualified and distributed bounding boxes for dense object detection. In *NeurIPS*, 2020. [1](#), [2](#), [3](#), [5](#), [6](#), [8](#), [11](#)
- [26] Yu Li, Tao Wang, Bingyi Kang, Sheng Tang, Chunfeng Wang, Jintao Li, and Jiashi Feng. Overcoming classifier imbalance for long-tail object detection with balanced group softmax. In *CVPR*, 2020. [2](#)
- [27] Tsung-Yi Lin, Piotr Dollár, Ross Girshick, Kaiming He, Bharath Hariharan, and Serge Belongie. Feature pyramid networks for object detection. In *CVPR*, 2017. [5](#), [11](#)
- [28] Tsung-Yi Lin, Priya Goyal, Ross Girshick, Kaiming He, and Piotr Dollár. Focal loss for dense object detection. In *ICCV*, 2017. [2](#), [5](#), [6](#), [11](#)
- [29] Tsung-Yi Lin, Michael Maire, Serge Belongie, James Hays, Pietro Perona, Deva Ramanan, Piotr Dollár, and C. Lawrence Zitnick. Microsoft coco: Common objects in context. In *ECCV*, 2014. [1](#), [2](#), [3](#), [5](#), [11](#)
- [30] Wei Liu, Dragomir Anguelov, Dumitru Erhan, Christian Szegedy, Scott Reed, Cheng-Yang Fu, and Alexander C.

- Berg. Ssd: Single shot multibox detector. In *ECCV*, 2016. 1, 2
- [31] Ze Liu, Yutong Lin, Yue Cao, Han Hu, Yixuan Wei, Zheng Zhang, Stephen Lin, and Baining Guo. Swin transformer: Hierarchical vision transformer using shifted windows. In *ICCV*, 2021. 6
- [32] Zhuang Liu, Hanzi Mao, Chao-Yuan Wu, Christoph Feichtenhofer, Trevor Darrell, and Saining Xie. A convnet for the 2020s. In *CVPR*, 2022. 6
- [33] Dhruv Mahajan, Ross Girshick, Vignesh Ramanathan, Kaiming He, Manohar Paluri, Yixuan Li, Ashwin Bharambe, and Laurens Van Der Maaten. Exploring the limits of weakly supervised pretraining. In *ECCV*, 2018. 2, 5
- [34] Kemal Oksuz, Baris Can Cam, Sinan Kalkan, and Emre Akbas. Imbalance problems in object detection: A review. *IEEE Transactions on Pattern Analysis and Machine Intelligence*, 43(10):3388–3415, 2020. 1
- [35] Wanli Ouyang, Xiaogang Wang, Cong Zhang, and Xiaokang Yang. Factors in finetuning deep model for object detection with long-tail distribution. In *CVPR*, 2016. 2
- [36] Jiangmiao Pang, Kai Chen, Jianping Shi, Huajun Feng, Wanli Ouyang, and Dahua Lin. Libra R-CNN: Towards balanced learning for object detection. In *CVPR*, 2019. 2
- [37] Joseph Redmon and Ali Farhadi. Yolov3: An incremental improvement. *arXiv preprint arXiv:1804.02767*, 2018. 1, 2, 5
- [38] Shaoqing Ren, Kaiming He, Ross Girshick, and Jian Sun. Faster R-CNN: Towards real-time object detection with region proposal networks. In *NeurIPS*, 2015. 1, 2, 5, 6, 11
- [39] Shuai Shao, Zeming Li, Tianyuan Zhang, Chao Peng, Gang Yu, Xiangyu Zhang, Jing Li, and Jian Sun. Objects365: A large-scale, high-quality dataset for object detection. In *ICCV*, 2019. 1
- [40] Abhinav Shrivastava, Abhinav Gupta, and Ross Girshick. Training region-based object detectors with online hard example mining. In *CVPR*, 2016. 2
- [41] Peize Sun, Rufeng Zhang, Yi Jiang, Tao Kong, Chenfeng Xu, Wei Zhan, Masayoshi Tomizuka, Lei Li, Zehuan Yuan, Changhu Wang, et al. Sparse R-CNN: End-to-end object detection with learnable proposals. In *CVPR*, 2021. 2, 6, 11
- [42] Benjamin W Tatler. The central fixation bias in scene viewing: Selecting an optimal viewing position independently of motor biases and image feature distributions. *Journal of vision*, 7(14):4–4, 2007. 1, 2
- [43] Zhi Tian, Chunhua Shen, Hao Chen, and Tong He. FCOS: Fully convolutional one-stage object detection. In *ICCV*, 2019. 2, 11
- [44] Antonio Torralba and Alexei A Efros. Unbiased look at dataset bias. In *CVPR*, pages 1521–1528, 2011. 1
- [45] Po-He Tseng, Ran Carmi, Ian GM Cameron, Douglas P Munoz, and Laurent Itti. Quantifying center bias of observers in free viewing of dynamic natural scenes. *Journal of Vision*, 9(7):4–4, 2009. 1, 2
- [46] Jiaqi Wang, Kai Chen, Shuo Yang, Chen Change Loy, and Dahua Lin. Region proposal by guided anchoring. In *CVPR*, 2019. 2
- [47] Tong Wang, Yousong Zhu, Chaoyang Zhao, Wei Zeng, Jinqiao Wang, and Ming Tang. Adaptive class suppression loss for long-tail object detection. In *CVPR*, 2021. 2
- [48] Wenhai Wang, Enze Xie, Xiang Li, Deng-Ping Fan, Kaitao Song, Ding Liang, Tong Lu, Ping Luo, and Ling Shao. Pyramid Vision Transformer: A versatile backbone for dense prediction without convolutions. In *ICCV*, 2021. 6
- [49] Saining Xie, Ross Girshick, Piotr Dollár, Zhuowen Tu, and Kaiming He. Aggregated residual transformations for deep neural networks. In *CVPR*, 2017. 6, 8
- [50] Ze Yang, Shaohui Liu, Han Hu, Liwei Wang, and Stephen Lin. Reppoints: Point set representation for object detection. In *ICCV*, 2019. 2
- [51] Haoyang Zhang, Ying Wang, Feras Dayoub, and Niko Sünderhauf. Varifocalnet: An iou-aware dense object detector. In *CVPR*, 2021. 1, 6
- [52] Shifeng Zhang, Cheng Chi, Yongqiang Yao, Zhen Lei, and Stan Z. Li. Bridging the gap between anchor-based and anchor-free detection via adaptive training sample selection. In *CVPR*, 2020. 3, 4
- [53] Xiaosong Zhang, Fang Wan, Chang Liu, Rongrong Ji, and Qixiang Ye. Freeanchor: Learning to match anchors for visual object detection. In *NeurIPS*, 2019. 3
- [54] Yifan Zhang, Bingyi Kang, Bryan Hooi, Shuicheng Yan, and Jiashi Feng. Deep long-tailed learning: A survey. *arXiv preprint arXiv:2110.04596*, 2021. 2
- [55] Zhi-Hua Zhou and Xu-Ying Liu. Training cost-sensitive neural networks with methods addressing the class imbalance problem. *IEEE Transactions on Knowledge and Data Engineering*, 18(1):63–77, 2005. 2, 5
- [56] Benjin Zhu, Jianfeng Wang, Zhengkai Jiang, Fuhang Zong, Songtao Liu, Zeming Li, and Jian Sun. Autoassign: Differentiable label assignment for dense object detection. *arXiv preprint arXiv:2007.03496*, 2020. 3
- [57] Chenchen Zhu, Fangyi Chen, Zhiqiang Shen, and Marios Savvides. Soft anchor-point object detection. In *ECCV*, 2020. 3
- [58] Chenchen Zhu, Yihui He, and Marios Savvides. Feature selective anchor-free module for single-shot object detection. In *CVPR*, 2019. 3
- [59] Xizhou Zhu, Han Hu, Stephen Lin, and Jifeng Dai. Deformable convnets v2: More deformable, better results. In *CVPR*, 2019. 8
- [60] Xizhou Zhu, Weijie Su, Lewei Lu, Bin Li, Xiaogang Wang, and Jifeng Dai. Deformable DETR: Deformable transformers for end-to-end object detection. *arXiv preprint arXiv:2010.04159*, 2020. 1, 6

## A1. Datasets

The experiments are conducted on the following 5 datasets, which are publicly available. The object distributions can be seen in Fig. A7.

**PASCAL VOC [10]** is one of the most widely used object detection benchmark under natural scenes, which contains 20 classes. We adopt the classical 07+12 training and testing protocol, i.e., the train set contains the union of VOC 2007 trainval and VOC 2012 trainval (totally 16551 images) and the test set contains VOC 2007 test (4952 images).

**MS COCO [29]** is another recently popular benchmark with much larger scale, containing 80 classes under natural scenes. We adopt COCO 2017 train (118K images) for training and COCO 2017 val (5K images) for evaluation.

**Face mask detection<sup>1</sup>**. With COVID-19 raging around the world, face mask detection is a widespread and necessary visual application. The dataset consists of 5,865 images for training and 1,035 images for testing. There are 2 classes. One is no mask and the other is mask.

**Fruit detection<sup>2</sup>** is widely used in industrial assembly line sorting and commodity classification. The dataset consists of 3,836 train images and 639 test images. 11 common fruits are included, e.g., apple, grape, and lemon.

**Helmet detection<sup>3</sup>** is a safety vision application that is often used in construction sites to detect whether personnel wear helmets. It contains 15,887 images for training and 6,902 images for testing. Two classes, head and helmet, are used.

## A2. More Experiments

### A2.1. Zone Evaluation on Detectors.

We provide zone evaluation to 6 object detectors, including Faster R-CNN [38] (two-stage), Cascade R-CNN [2] (multi-stage), DETR [4] (transformer-based sparse detector), Sparse R-CNN [41] (two-stage sparse detector), RetinaNet [28] (one-stage), and FCOS [43] (one-stage). These detectors adopt the same backbone network ResNet-50 [17]. For CNN-based detectors, FPN [27] is equipped as the neck network and a  $1 \times$  training schedule is adopted (12 epochs). While for DETR, the default 150 epochs training schedule is adopted. The number of evaluation zones  $n$  is set to 10, where the zone ranges are  $(r_i, r_j) = (0, 0.05j)$  in Fig. A8(a), and  $(r_i, r_j) = (0.05i, 0.5)$  in Fig. A8 (b),  $i \in \{0, 1, \dots, 9\}$ ,  $j \in \{1, 2, \dots, 10\}$ . Fig. A8(a) shows that when  $r_j < 0.5$ , all the ZPs are less than the traditional

<sup>1</sup><https://www.kaggle.com/datasets/parot99/face-mask-detection-yolo-darknet-format>

<sup>2</sup><https://www.kaggle.com/datasets/eunpyohong/fruit-object-detection>

<sup>3</sup><https://www.kaggle.com/datasets/vodan37/yolo-helmethead/metadata>

one ( $r_j = 0.5$ ). On the other hand, Fig. A8(b) shows a ZP increasing tendency as the evaluation zones shrink to the image center. This indicates that the detectors perform better in the central zone than in most border area. Particularly, we note that the sparse detectors, DETR and Sparse R-CNN favor more in the central zone ( $r_i > 0.3$ ), as shown in Fig. A8(b).

### A2.2. A Close Look at Detectors' Spatial Bias

As mentioned in Section 1 of the main paper, we found some clues about the detectors' spatial bias when computing the AP scores for different zones. This object distribution bias makes it difficult for detectors to have consistent performance across different image zones. To further demonstrate this, we create a simple yet heuristic experiment by manually reducing the object supervision signals in a certain zone. We conduct experiments using the popular Gfocal [25] detector under the classic PASCAL VOC 07+12 [10] protocols.

We first evenly divide the whole image zone into two (left and right) halves. Then, there are four pipeline settings for comparison:

1. "left-0" detector: we train the network by discarding all the objects whose centers lie in the left zone of the image.
2. "right-0" detector: analogous to "left-0" detector by discarding the right zone objects.
3. "left-1" detector: we only assign 1 positive sample for every left zone object.
4. "right-1" detector: the opposite settings to "left-1".

All the four detectors differ only in sampling process. During training, horizontal flip with a probability of 0.5 is used to ensure that both left and right objects participate in the model training. The evaluation is conducted on the left zone, the right zone and the whole image separately.

Table A1 shows the quantitative results and we have the following observations.

- **Imbalanced sampling of training samples causes severe spatial disequilibrium.** It can be seen that the detection performance of the "left-0" detector in the left zone is very poor, 13.1 ZP worse than that in the right zone. This turns out surprisingly that the detector cannot uniformly perform across the zones. If we adopt the horizontal flip during testing, it will be completely reversed for the left zone and the right one. The same observation can be seen from the "right-0" detector. This implies that the detection performance heavily depends on the positions of objects. And the detector is good at detecting objects in the favor zone, simply because it receives much more supervision signals and therefore be endowed much better detection ability during training. We also visualize the detection quality in Fig. A9, where the cat shifts from left to

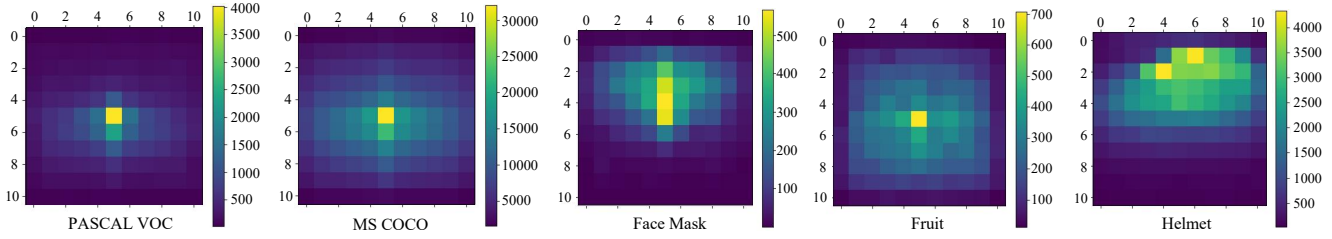


Figure A7. The photographer’s bias in the 5 object detection datasets. We count the center points for all the ground-truth boxes. The images are divided into  $11 \times 11$  zones.

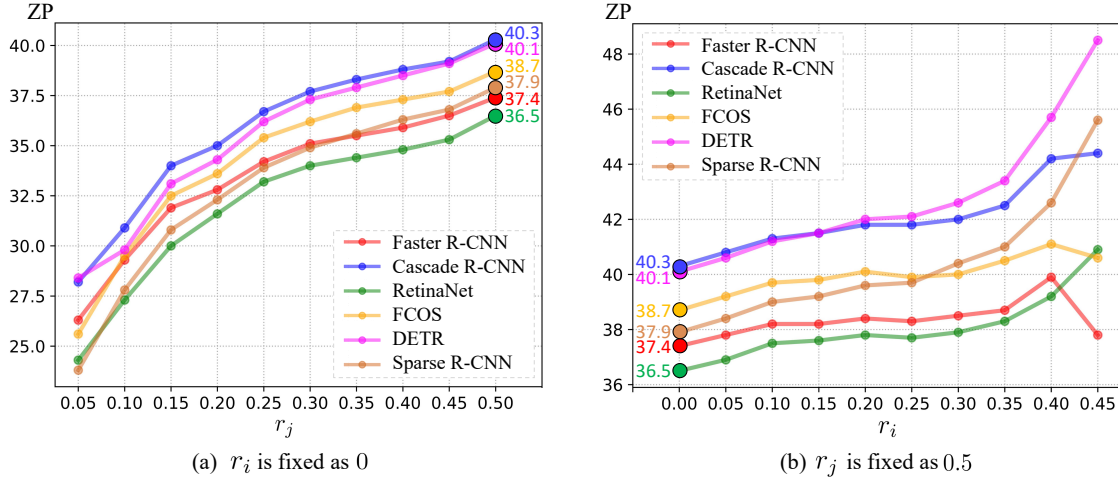


Figure A8. The ZP against the zone range  $(r_i, r_j)$ , where  $r_i = 0.05i$ ,  $r_j = 0.05j$ , and  $i, j \in \{0, 1, 2, \dots, 10\}$ . All the 6 detectors adopt the popular ResNet-50. The results are reported on the COCO val 2017.

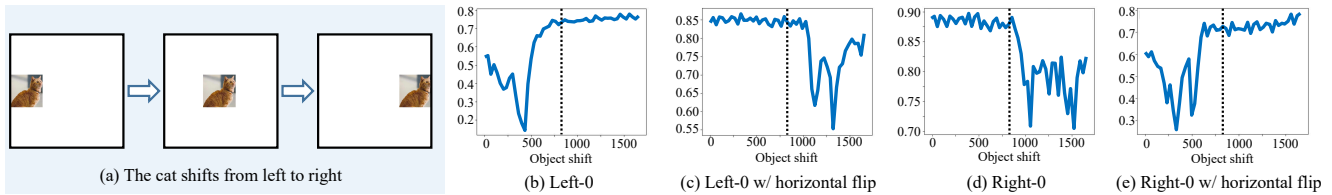


Figure A9. **The cat is not that cat.** The curves (b-e): Product of classification score and IoU (between detected box and the ground-truth box) as the cat shifting from left to right. Imbalance sampling causes severe spatial bias, that the cat in the disfavor zone cannot be detected as good as in the favor zone. If we flip the cat to the favor zone, the detection quality backs to normal immediately.

right. It can be seen that the detection quality will significantly drop when the cat is not at the favor zone. If we flip the cat to the favor zone, the detection quality backs to normal immediately. In Fig. A10, one can see that the detector produces very weak classification responses for the cats in the disfavor zone. Such spatial bias has a great impact on the robustness of detection applications.

- **Traditional metrics fail to capture spatial bias.** One can see that the “left-0” detector produces a 40.9 full map ZP (traditional AP), which is unable to provide a reference for where and how much the performance drops. Our zone metrics provide more meaningful in-

formation about the detection performance.

- **Increasing training samples for the disfavor zone shrinks the performance gap between zones.** Table A1 also shows us promising results that the performance gap between the two zones can be significantly shrunk by simply increasing positive samples for the disfavor zones. And it should be noted that the performance gap still exists as the sampling remains imbalanced.

According to the above analysis, we indicate that the spatial bias not only exists, but also plays a nonnegligible role in gauging the performance of object detectors.

H Flip	Left-0 detector			Left-1 detector			Right-0 detector			Right-1 detector		
	ZP@left	ZP@right	ZP@full	ZP@left	ZP@right	ZP@full	ZP@left	ZP@right	ZP@full	ZP@left	ZP@right	ZP@full
	28.9	42.0	40.9	42.8	44.5	49.3	42.8	27.2	40.5	45.7	41.0	49.2
✓	42.3	28.8	40.8	45.0	41.7	49.5	27.6	42.3	40.6	42.0	45.3	49.0

Table A1. **Detector’s spatial bias.** “Left-0”: discard all the left zone objects. “Left-1”: keep only 1 positive sample for each left zone object. The left/right/full zone ZP is reported. “Right-0”: discard all the right zone objects. “Right-1”: keep only 1 positive sample for each right zone object. The left/right/full zone ZP is reported. “H Flip”: testing with horizontal flip. The detector performs extremely imbalanced between the two zones. Also, increasing training samples for the disfavor zones will shrink the performance gap.

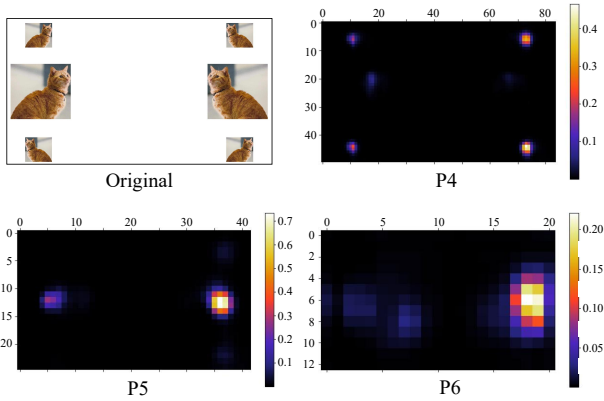


Figure A10. Visualization of the class score on P4, P5 and P6 FPN levels. The detector is trained by discarding all the objects whose centers lie in the left zone of the image. The detector produces very weak classification responses for the cats on the left zone.

### A2.3. Visualization of Detection.

We visualize the detection results of SELA in Fig. A11. Our method can significantly improve the detection performance for the border zone. We believe the further exploration about spatial equilibrium is clearly worthy and important for the robust detection applications in the future.

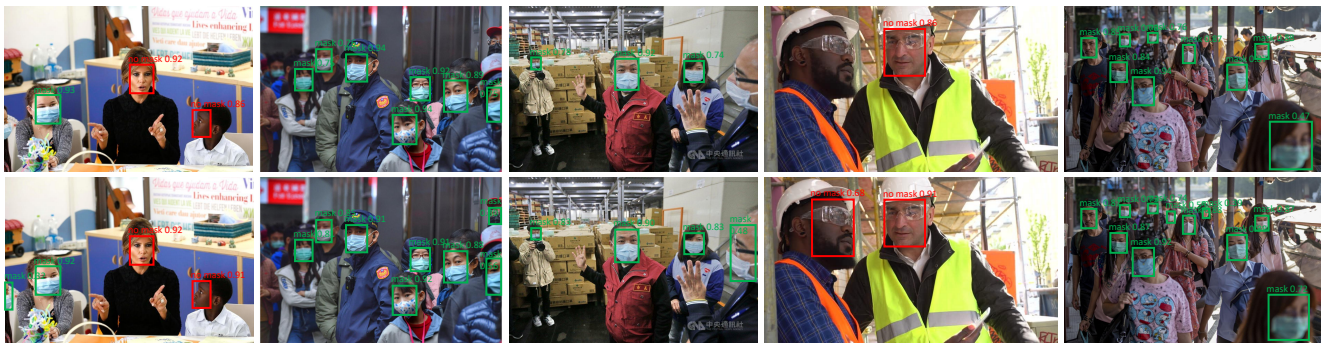


Figure A11. Illustration of detection results for GFocal (first row) and GFocal + SELA (second row). Zoom in for a better view.